



Interdiffusion behavior between Cr and Zr and its effect on the microcracking behavior in the Cr-coated Zr-4 alloy

Ji-Shen Jiang¹ · Dong-Qing Wang¹ · Ming-Yue Du¹ · Xian-Feng Ma¹ ·
Chen-Xue Wang¹ · Xiu-Jie He¹

Received: 7 September 2021 / Revised: 3 November 2021 / Accepted: 5 November 2021 / Published online: 6 December 2021
© The Author(s), under exclusive licence to China Science Publishing & Media Ltd. (Science Press), Shanghai Institute of Applied Physics, the Chinese Academy of Sciences, Chinese Nuclear Society 2021

Abstract High-temperature chromium (Cr)-zirconium (Zr) interdiffusion commonly occurs in Cr-coated zircalloys applied for enhanced accident-tolerant fuel (ATF) claddings. Such interdiffusion changes the interfacial microstructure and thus the fracture mechanism of the coating under external loading. In this study, the interdiffusion behavior in a magnetron sputtered Cr coating deposited on a Zr-4 alloy was studied in a vacuum environment at 1160 °C. In addition, the effect of interdiffusion on the microcracking behavior of the Cr coating was determined by in situ three-point bending tests. The experimental results show that the interdiffusion behavior resulted in the formation of a ZrCr₂ layer, accompanied by the consumption of Cr coating and interfacial roughening. The growth of the diffusion layer followed a nearly parabolic law with respect to annealing time, and the residual stress of the annealed coating decreased with increasing

annealing time. Under external loading, a large number of cracks were generated in the brittle interlayer, and some interfacial cracks were formed and grew at the ZrCr₂/Zr-4 interface. Despite the remarkable microcracks in the ZrCr₂ layer, the vacuum-annealed Cr coating has significantly fewer cracks than the original coating, mainly because of the recrystallization of the coating during annealing.

Keywords Accident-tolerant fuel · Surface coating · Interdiffusion · Three-point bending test · Crack propagation

1 Introduction

Nuclear reactor safety in severe accident scenarios has drawn worldwide attention since the Japan Fukushima nuclear accident in 2011 [1, 2]. Zircaloy has been utilized as a nuclear fuel cladding material since the 1960s. However, in an extreme environment under accident conditions, zircaloy claddings suffer from rapid oxidation and severely depleted mechanical properties, causing hydrogen generation and catastrophic failure. Hence, in recent years, it has attracted worldwide interest to develop enhanced accident-tolerant fuel (ATF) cladding materials to enhance the accident resistance of claddings during beyond-design-basis scenarios [1–5]. Among several reported potential methods, surface coating with superior oxidation resistance deposited on the zircaloy cladding has been considered one of the near-term solutions for next-generation ATF systems [2, 6].

A metallic Cr coating was considered in this study because of its excellent oxidation resistance and outstanding mechanical properties at elevated temperatures [7–10].

This work was sponsored by the Guangdong Major Project of Basic and Applied Basic Research (No. 2019B030302011), National Natural Science Foundation of China (Nos. 52005523, U2032143, 11902370), International Sci & Tech Cooperation Program of Guangdong Province (No. 2019A050510022), Key Research Project of Guangdong Province (Nos. 2019B010943001 and 2017B020235001), China Postdoctoral Science Foundation (Nos. 2019M653173 and 2019TQ0374), and the Fundamental Research Funds for the Central Universities, Sun Yat-sen University (No. 2021qntd12).

✉ Xian-Feng Ma
maxf6@mail.sysu.edu.cn

✉ Xiu-Jie He
hexiujie@mail.sysu.edu.cn

¹ Sino-French Institute of Nuclear Engineering and Technology, Sun Yat-Sen University, Zhuhai 519082, China

Under high-temperature accident conditions, outer oxidation occurs in the coating, which forms a chromium oxide layer on the coating surface, preventing further oxidation of the coating and enhancing the oxidation resistance of the substrate [11]. Brachet et al. [12–14] found that the oxidation of the physically vapor-deposited Cr-coated Zr substrate was evidently slower than that of the uncoated substrate. Furthermore, the growth of the outer Cr_2O_3 layer could be described by nearly parabolic oxidation kinetics in the 800–1300 °C steam environment. As reported by Yeom et al. [15], a cold-sprayed Cr coating led to a remarkable reduction in the oxidation rate compared to the uncoated Zr substrate in the 1310 °C steam environment. Interdiffusion between Cr and Zr occurs simultaneously with outer oxidation to form an intermetallic layer (ZrCr_2 layer). Yang et al. [16] found that the intermetallic layer growth was controlled by a nearly parabolic law in an inert gas environment, and its growth rate was strongly correlated with the temperature and deposition methods. The presence of the ZrCr_2 layer might be beneficial for reducing coating/substrate thermal mismatch, but it might also introduce microcracking in this brittle layer, lowering the interfacial adhesion [17, 18]. Moreover, the diffusion of Cr also leads to the consumption of the Cr coating, which might be a risk to the effective protection of the underlying substrate [16].

The formation of ZrCr_2 and the coating consumption could change the geometry and strength of the coated zirconium alloy, further altering the cracking mode under external loading. As reported by Jiang et al. [19, 20], at low temperatures, the Cr coating was too brittle to form numerous channel cracks on the surface of the coating under tension, but its crack resistance improved remarkably as the temperature reached 400 °C. Moreover, the cracking modes changed from brittle to ductile with increasing temperature. However, our recent study [21] showed that the cracking modes of Cr coating, oxidized and vacuum-annealed above 1100 °C for 1 h, were evidently different from those of the as-deposited coating. Crack formation occurred in the brittle diffusion layer rather than in the Cr coating under external loading. However, the intrinsic mechanism of the growth of the diffusion layer and its effect on the cracking behavior remains unclear.

In this work, the interdiffusion behavior between Cr and Zr in a Cr-coated-Zr-4 substrate system was investigated in a vacuum environment at 1160 °C. The growth of the diffusion layer, coating consumption, and evolution of the interfacial morphology were further investigated. Moreover, three-point bending tests were conducted to study the interdiffusion effect on the cracking behavior in real time, and the difference in the cracking mode between the as-deposited and vacuum-annealed Cr coatings was determined.

2 Experimental

2.1 Materials, heat-treatment processes, and characterization

A $20 \times 20 \times 2 \text{ mm}^3$ rectangular Zr-4 alloy was selected as the substrate material. Before the coating deposition, the substrate surfaces were polished using #1500 SiC papers and then ultrasonically cleaned. Subsequently, Cr coatings were deposited on the Zr-4 substrates using the magnetron sputtering technique. The detailed deposition process is reported by Jiang et al. [21].

To study the interdiffusion-induced microstructure evolution, several coated samples were subjected to vacuum annealing. To prevent high-temperature oxidation, the coated samples were sealed in vacuum quartz packages before heating. Subsequently, the samples in the quartz packages were placed in a muffle furnace to undergo isothermal exposure after the furnace temperature reached 1160 °C, and then naturally air cooled after removal from the furnace. Notably, owing to the limited vacuum in the quartz packages, a small amount of oxygen may remain. The samples were annealed at different times ranging from 15 min to 4 h.

The residual stress of the original Cr coatings and vacuum-annealed Cr coatings were estimated using the $2\theta \sin^2\psi$ X-ray diffraction (XRD) technique. Detailed information on the testing process was reported by Yang et al. [16]. The microstructures of the coatings were studied by scanning electron microscopy (SEM). The elemental distributions of Zr and Cr in the coated samples were determined by energy-dispersive X-ray spectroscopy (EDS). The phase compositions of the vacuum-annealed samples were evaluated using XRD analyses. Moreover, the grain size and orientation of the original and vacuum-annealed Cr coatings were identified by electron backscatter diffraction (EBSD, EDAX) measurements.

2.2 In situ three-point bending tests

To investigate the interdiffusion effect on the crack evolution in Cr coatings, the original and vacuum-annealed coatings underwent three-point bending tests in a mechanical testing system with SEM. Various mechanical tests at room/high temperatures were conducted using this system [19, 20, 22]. The three-point bending tests provide more detailed information on the formation and evolution of both channel and interfacial cracks in real time than the in situ tensile tests. The three-point bending samples were cut from a Zr-4 alloy plate (which was also used for preparing rectangular samples for microstructure characterization, as mentioned in Sect. 2.1) using a spark-

discharging machine. These samples underwent the same pre-treatment and coating processes as the rectangular samples. After deposition, the coated three-point bending samples were vacuum-annealed. Subsequently, the observing surface was ground to reveal the cross section. Prior to testing, the coated specimen was fastened to the testing system. Then, a bending test was performed, and the displacement rate remained constant at 0.005 mm/s. To acquire the load (P)-deflection (w) relation, the force and displacement of the indenter were logged by a computer. Furthermore, when the deflection reached the required magnitude, the bending test was paused to obtain SEM images of the cracking behavior in the coating by setting the scanning electron microscope above the sample. Finally, the bending test was stopped when the after-target deflection was reached.

3 Results and discussion

3.1 Interdiffusion behaviors

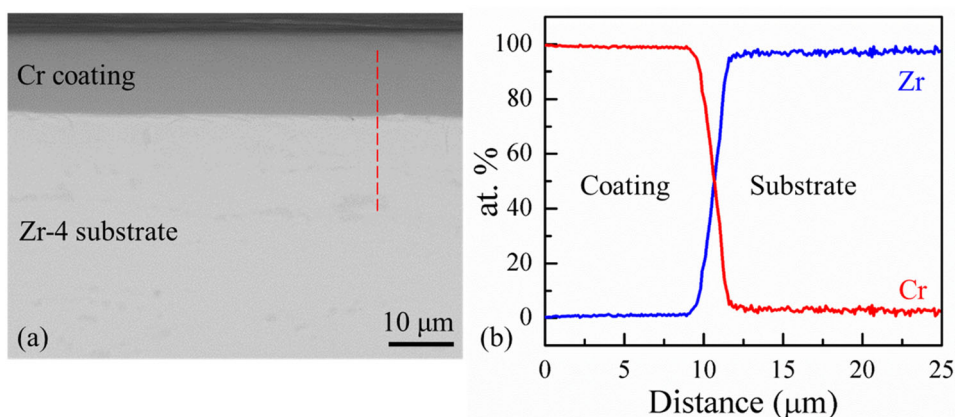
Figure 1 presents the cross-sectional morphology and EDS line scan results of the original Cr-coated sample. As shown in Fig. 1a, the Cr coating is 13 μm thick and possesses highly dense microstructures without microvoids at the interface. Notably, there is a thin element transition area at the interface in Fig. 1b, which was caused by the smoothing effect due to the limited spatial resolution of EDS, related to different factors such as the stray electrons, beam broadening, and step size. During line scanning, the stray electrons could induce X-rays from both sides of the interfaces when the spot neared the interface, causing a gradual variation in the intensities of Cr and Zr.

Figure 2 displays the cross-sectional appearance and EDS results of the sample vacuum-annealed for 15 min. No oxide layer formed on the vacuum-annealed coating surface. In addition, a thin diffusion layer formed at the

interface. From Fig. 1b and the transmission electron microscopy results reported by Brachet et al. [12] and Jiang et al. [21], the diffusion layer was determined to be an intermetallic ZrCr_2 layer possessing the Laves phase. As shown in the SEM and EDS results, numerous scattered precipitates appeared in the area beneath the ZrCr_2 layer, but its composition was not determined with certainty because the resolution of the SEM-EDS map or line scan was limited. These micron-sized Cr-rich precipitates were considered to be a ZrCr_2 or/and $\text{Zr}(\text{Fe}, \text{Cr})_2$ phase, which formed because of Cr precipitation in the substrate during the cooling period [15, 16, 23]. Furthermore, the scattered Cr-rich precipitates were mainly located in the area with a relatively long distance from the coating/substrate interface, instead of the area near the interface, as was reported by Yang et al. [16]. The authors considered that the non-uniform distribution of the Cr-rich precipitates was attributed to the presence of the oxygen-stabilized $\alpha\text{-Zr}(\text{O})$ phase in the area underneath the ZrCr_2 layer. Although a vacuum environment was provided in the sealed quartz packages, a small amount of oxygen may remain. At high temperatures, oxygen might penetrate the Zr-4 substrate, which promotes a β -to- α phase transformation. As the $\alpha\text{-Zr}(\text{O})$ phase had a lower solubility of Cr than the $\beta\text{-Zr}$ phase, the Cr-rich spots mainly precipitated in the $\beta\text{-Zr}$ phase [24].

When the annealing time was longer, the diffusion layer became thicker, and the more significant the separated Cr precipitates (see Fig. 3). As the high-temperature exposure continued, Cr and Zr constantly reacted to form intermetallic ZrCr_2 , which thickened the diffusion layer. However, owing to the local uneven diffusion rate at the interface, the ZrCr_2 layer had an uneven thickness. In Fig. 4, the cross-sectional appearance and elemental distribution of the Cr coating annealed for 2 h followed a similar trend to that annealed for 1 h; namely, the interface became rougher and the ZrCr_2 layer became thicker. In addition, significant consumption of the Cr coating

Fig. 1 (Color online) **a** SEM image of the cross-sectional morphology and **b** the corresponding EDS line scan of the original Cr-coated sample



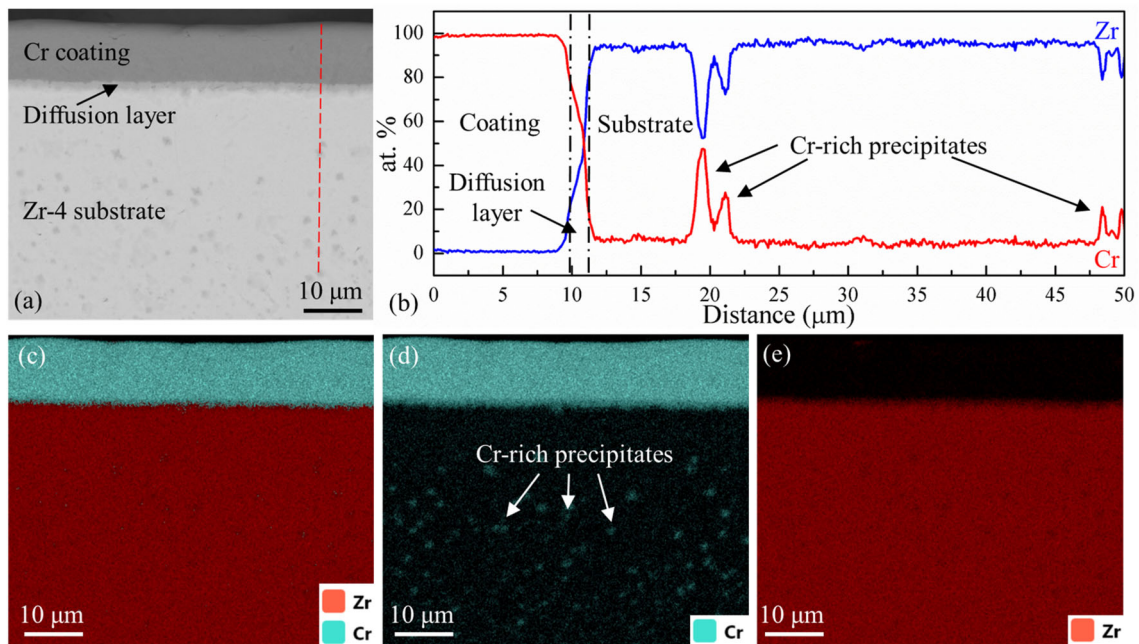


Fig. 2 (Color online) **a** SEM image of the cross-sectional microstructure, **b** results of the EDS line scan, and **c–e** EDS maps of the sample vacuum-annealed for 15 min

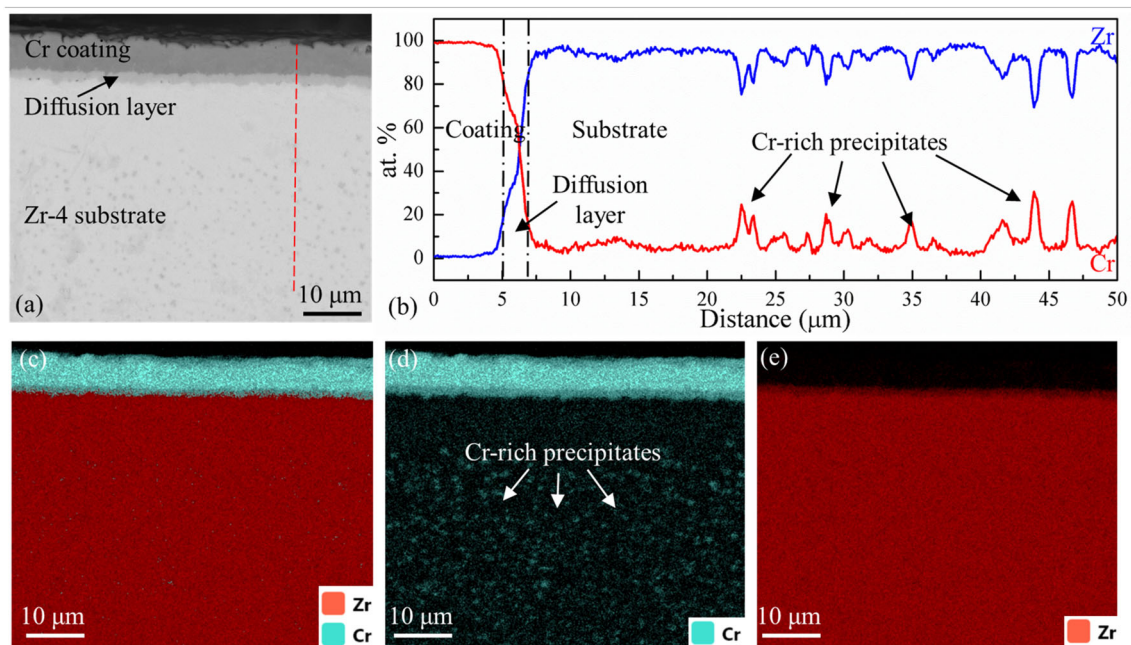


Fig. 3 (Color online) **a** SEM image of the cross-sectional microstructure, **b** results of the EDS line scan, and **c–e** EDS maps of the sample vacuum-annealed for 1 h

occurred simultaneously owing to the presence of the $ZrCr_2$ layer and continual Cr diffusion.

Figure 5 displays the cross-sectional appearance and EDS results of the sample vacuum-annealed for 4 h. After a long diffusion time, the remaining Cr coating became thin due to remarkable Cr diffusion. Therefore, the $ZrCr_2$

thickness was even larger than that of the coating, and the Cr/ $ZrCr_2$ /Zr-4 interfaces became significantly rougher because of the uneven diffusion rate. As shown in Fig. 5, a local maximum Zr concentration appears in the diffusion layer. This phenomenon was believed to be caused by Zr diffusing into the coating, considering that the solubility of

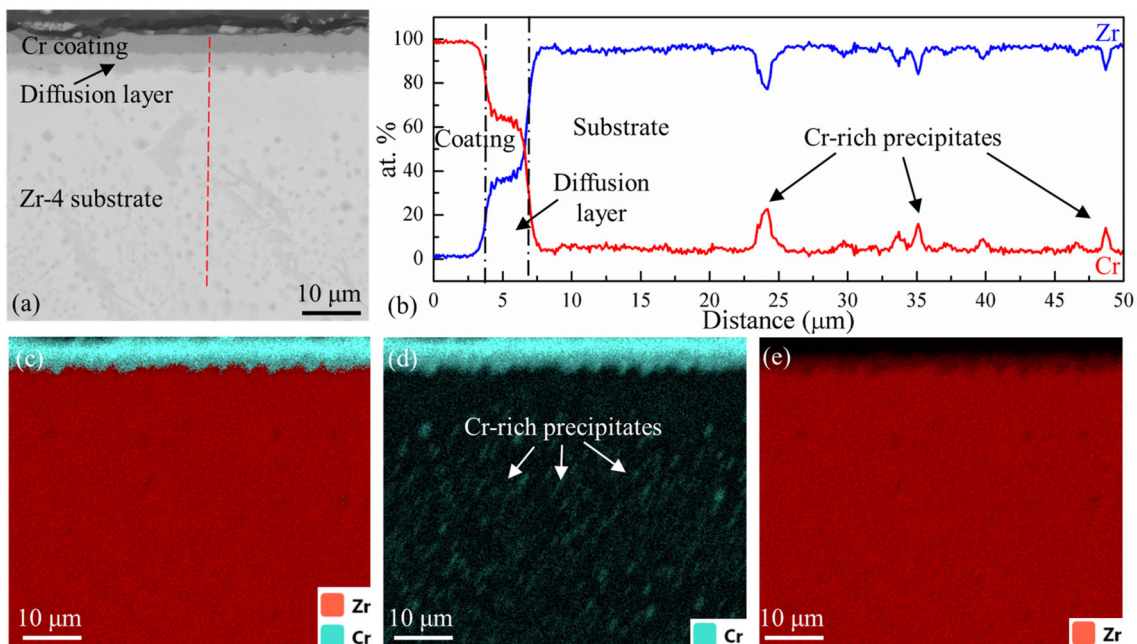


Fig. 4 (Color online) **a** SEM image of the cross-sectional microstructure, **b** results of the EDS line scan, and **c–e** EDS maps of the sample vacuum-annealed for 2 h

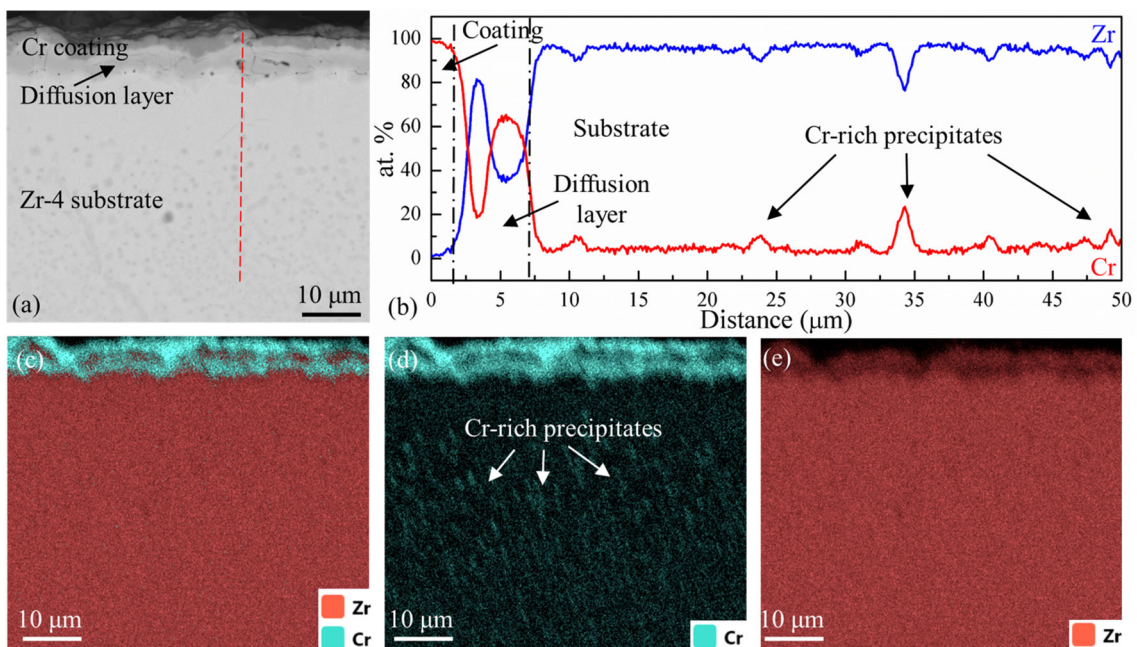


Fig. 5 (Color online) **a** SEM image of the cross-sectional microstructure, **b** results of the EDS line scan of the red line in **a**, and **c–e** the corresponding EDS maps of the Cr-coated Zr-4 substrate annealed for 4 h

the Zr atoms in the Cr coating was much lower than that of the Cr atoms in the β -Zr phase [12, 16, 17]. In addition, Zr was generally enriched in paths along the grain boundaries of the coating [12, 16, 17], which is not consistent with the presented results. Despite this, a small amount of Zr might also have dissolved into the Cr coating. Moreover, it was

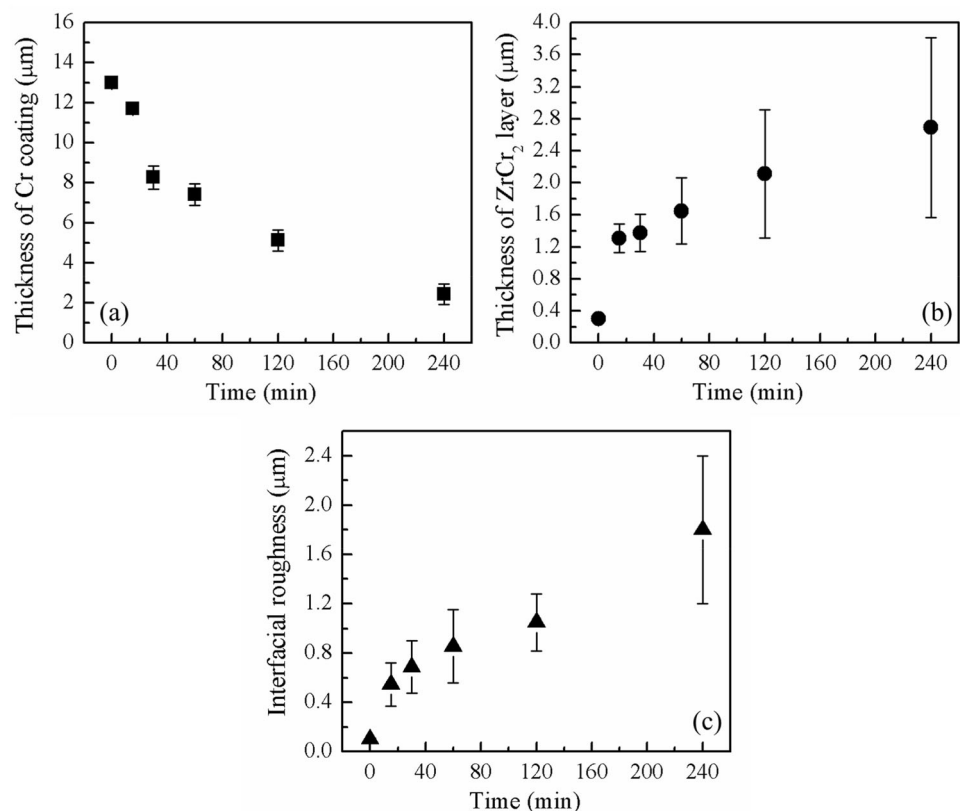
reported that the Cr in the ZrCr_2 phase had a much lower diffusion coefficient than Cr in the Zr substrate [16]. The amount of Cr that precipitated from the ZrCr_2 to the Zr-4 layer was greater than that from the Cr coating to the ZrCr_2 layer after extended annealing time. From this point, the atomic percentage of Cr decreased locally in the interlayer,

which increased the atomic percentage of Zr (see Fig. 5(b)). Moreover, some microvoids occurred near the interface, which were formed due to the Kirkendall effect, where the differences in the Cr and Zr diffusion rates caused a back diffusion of vacancies at the interfaces [12, 16].

According to the above results, the thickness of all layers, as well as the interfacial roughness, are functions of the annealing time. Figure 6 summarizes their evolution with respect to the annealing time by counting at least three samples for each annealing condition. As shown in Fig. 6a, the Cr coating thickness decreased at a lower rate with the annealing time, indicating that the consumption rate of Cr was high during the initial period of annealing because of the rapid Cr-Zr chemical reaction and the precipitation of Cr atoms into the substrate; however, it decreased during the late period of annealing because of the lower chemical reaction rate between Cr and Zr. In Fig. 6b, the ZrCr₂ layer thickened at a lower rate with the annealing time, which roughly followed a parabolic law, as reported in [15, 16]. During the initial period of annealing, the fast reaction-diffusion process between Cr and Zr played a dominant role in the formation of the diffusion layer. During the late period, the growth of the ZrCr₂ layer became diffusion-controlled, accompanied by a decrease in the interdiffusion coefficient. Meanwhile, the extent of Cr atoms diffusing

from the ZrCr₂ layer into the Zr substrate is greater than that from the coating to the ZrCr₂ layer, slowing down the growth rate of the ZrCr₂ layer during the late period [24]. It is worth noting that the ZrCr₂ layer appeared to be slightly thicker than that in the Cr coating produced by cold spray and magnetron sputtering techniques with other deposition parameters [15, 16]. The deposition process and parameters significantly affected the diffusion rate of the ZrCr₂ layer, which will be further studied in future work. Moreover, in Fig. 6c, the interfacial roughness also increased with the annealing time, indicating that the diffusion process became more irregular at the interface. During the diffusion process, the ZrCr₂ layer growth direction was generally normal with respect to the rough interface, leading to an increase in the interfacial roughness [16]. In addition, the local interfacial stress (corresponding to the thermal mismatch and creep effect) might also result in an irregular diffusion rate and thus an increased interfacial roughness [25]. Furthermore, the intergranular diffusion rate was generally larger than the transgranular diffusion; thus, Zr-Cr interdiffusion was prone to occur at the grain boundaries of the ZrCr₂ layer, further roughening the coating/substrate interface. Based on Figs. 6a and b, the remaining ZrCr₂-coating layer was thinner than the as-deposited coating. The thickness loss became more severe with increasing

Fig. 6 **a** Thickness of Cr coating vs. annealing time, **b** thickness of ZrCr₂ layer vs. annealing time, and **c** interfacial roughness vs. annealing time



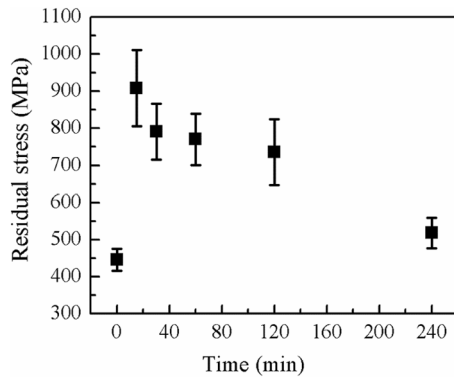


Fig. 7 Compressive residual stress in the Cr coating vs. annealing time

annealing time. This phenomenon is mainly attributed to continual Cr precipitation into the substrate.

Figure 7 presents the residual stress σ_r in the Cr coating before and after annealing at different times. After deposition, the Cr coatings had a compressive σ_r of -446 MPa. During high-temperature annealing, the residual stress produced during the deposition was strongly released. Nevertheless, because of the thermal mismatch between all layers, a large thermal stress was generated in the Cr coating upon cooling from 1160 °C to room temperature. In Fig. 7, the compressive residual stress of the 15 min vacuum-annealed Cr coating reached -908 MPa. After extended high-temperature annealing, the residual stress in

the Cr coating decreased significantly and reached a minimum value of -518.1 MPa in the Cr coating annealed for 4 h. The decrease in the residual stress is mainly due to the decrease in the thermal mismatch stress in the Cr coating. After further annealing, the Cr coating became thinner and the ZrCr_2 layer became thicker. Considering that the elastic modulus (173.2 GPa [26]) and thermal coefficient ($6.48 \times 10^{-6} \text{ K}^{-1}$ [27]) of the ZrCr_2 layer fall in the range between the magnitudes of the Cr coating (280 GPa [28] and $6.5 \times 10^{-6} \text{ K}^{-1}$ [17]) and the Zr-4 substrate (110 GPa [29] and $5.77 \sim 7.62 \times 10^{-6} \text{ K}^{-1}$ [17]), respectively, the ZrCr_2 layer could be regarded as a transition layer to reduce the thermal mismatch. Thus, the thickening of the ZrCr_2 layer upon effective annealing reduced the thermal stress, which decreased the residual stress in the vacuum-annealed Cr coating. Furthermore, during the cooling process, the Zr substrate also undergoes a β to α phase transformation, which results in a transformation-induced plasticity (TRIP) effect at temperatures between 900 and 800 °C, greatly releasing the stress caused by thermal mismatch in the coated sample [30, 31].

3.2 Recrystallization in the Cr coating

High-temperature annealing not only generated interdiffusion, but also caused variations in the microstructure of the Cr coating system. Figure 8 shows the EBSD results

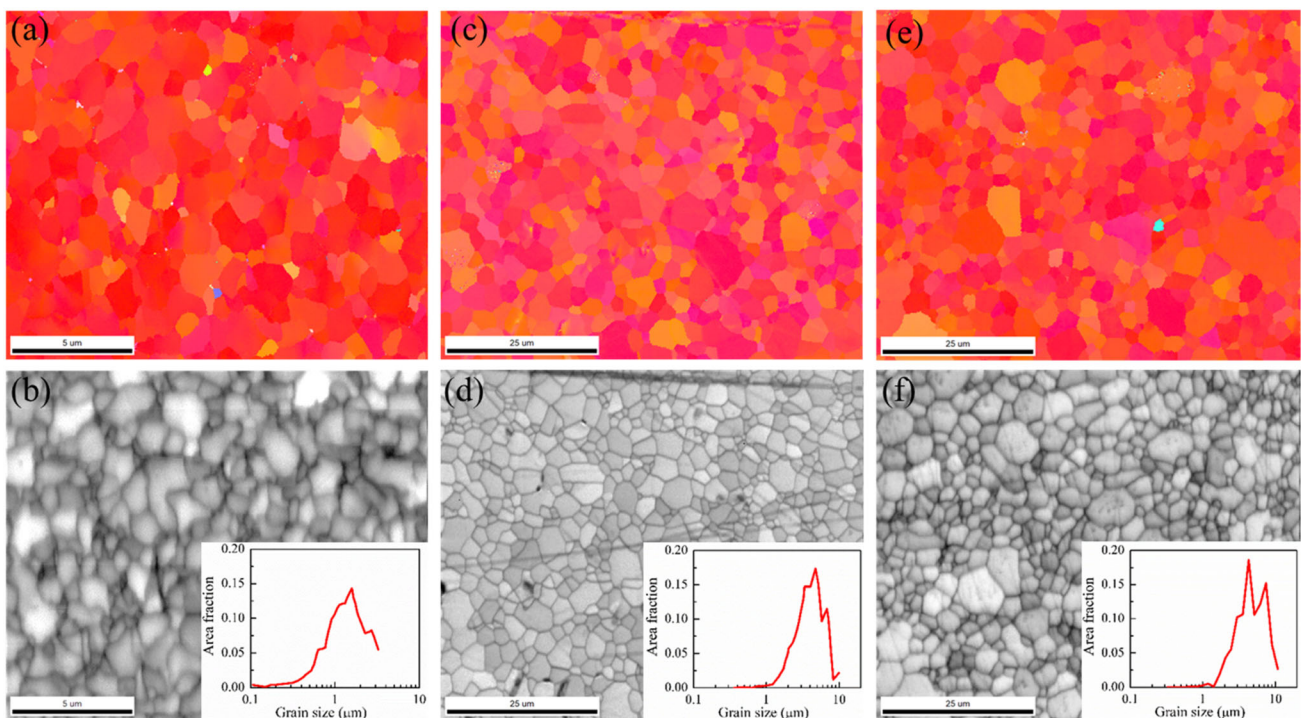


Fig. 8 (Color online) EBSD results of the coating surfaces: **a** orientation map and **b** IQ image of the original coating, **c**) orientation map and **d**) IQ image of the coating vacuum-annealed for 15 min, and **e**) orientation map and **d**) IQ image of the coating vacuum-annealed for 1 h

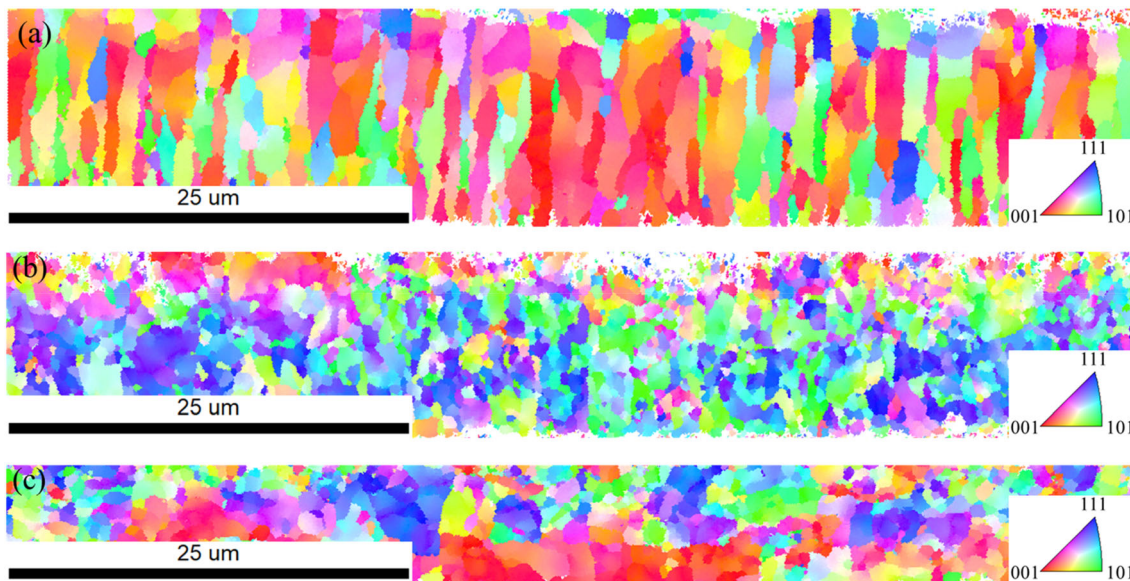


Fig. 9 (Color online) EBSD orientation maps of the cross sections of the **a** original Cr coating, and the Cr coating **b** vacuum-annealed for 15 min, and **c** vacuum-annealed for 1 h

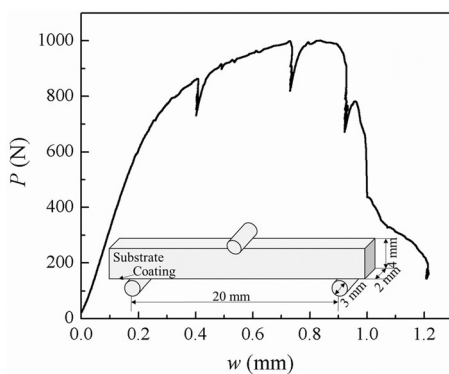


Fig. 10 **a** P - w curve of the sample vacuum-annealed for 1 h during the bending test

of the surfaces of the original and vacuum-annealed Cr coatings. In Figs. 8a and b, an intensive (001) texture occurred in the original Cr coating in the direction perpendicular to the interface. Based on the IQ image in Fig. 8b, the grain size of the Cr coating reached an average of 1.49 μm . After annealing for 15 min and 1 h, the grain sizes reached 4.34 and 5.11 μm , respectively. Recrystallization was observed in the Cr coating upon annealing; however, this did not obviously change the intensities of the textures. Note that the EBSD results of the Cr coatings annealed for 2 and 4 h are not presented because the severe Cr consumption decreased the thickness of the Cr coating, resulting in very low calibration rates during EBSD testing. Despite this, the Cr coating annealed for a longer time presumably possessed larger grains with strong textures.

Figure 9 shows the EBSD maps of the cross sections of the original and vacuum-annealed Cr coatings. Clearly, the

original Cr coating had columnar grains, which is a common feature in the coatings prepared by magnetron sputtering and other physical vapor deposition techniques [12, 21, 32]. However, as shown in Fig. 9b, it was surprising that after annealing for 15 min, equiaxial grains occurred in the Cr coating which were transformed from the original columnar grains that resulted from recrystallization at high temperatures. As shown in Fig. 9c, after annealing for 1 h, the coating thickness declined and the equiaxial grain grew to some extent. The equiaxial grains were presumably constantly coarsened during long-time annealing before the coating was consumed.

3.3 In situ three-point bending test

The above results suggest that high-temperature vacuum annealing evidently changed the microstructure of the coating, leading to the formation of an intermetallic layer and recrystallization in the Cr coating. The microstructural evolution may significantly change the mechanical properties and crack resistance of the Cr coating. Figure 10 presents the P - w curve of the coating vacuum-annealed for 1 h during the bending test. As shown in Fig. 10, P increased linearly when $w < 0.2$ mm, and increased slowly when $0.2 \leq w \leq 0.85$ mm. When $w > 0.85$ mm, the loading dropped significantly because of the macrocracks which formed and propagated rapidly in the Zr-4 substrate. Considering that the test was paused to acquire SEM images, some small drops in the load were observed, but they did not affect the overall mechanical behavior.

Figure 11 presents the results of the cracking behavior in the 1 h vacuum-annealed Cr coating during the bending

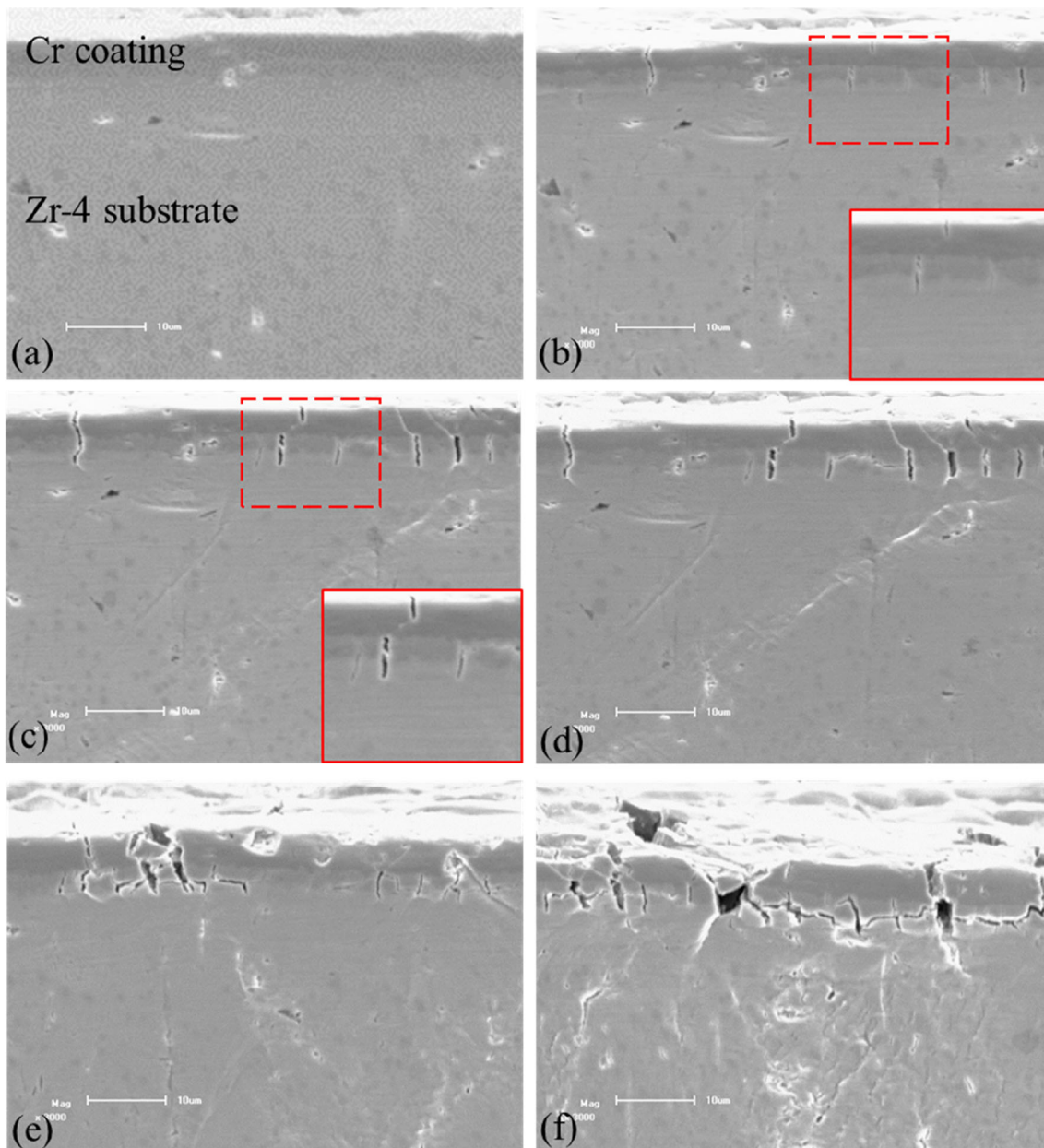


Fig. 11 SEM results showing crack evolution in the Cr coating vacuum-annealed for 1 h during bending at w of **a** 0.000 mm, **b** 0.405 mm, **c** 0.734 mm, **d** 0.926 mm, and **e**, **f** 1.210 mm. Insets show magnified views of the sections in red boxes

test. As shown in Fig. 11b, most of the microcracks appear at the interface, and few cracks penetrate across the coating when w reaches 0.405 mm. In addition, as shown in the magnified view in Fig. 11b, few microcracks were observed on the coating surface. Under continuous loading, more microcracks were formed at the coating/substrate interface. Remarkable slip lines were generated at the crack tips owing to large deformations. Despite this, the cracks that formed from the interface and the surface barely coalesced, which may be blocked by the grain boundaries in the Cr coatings. In Figs. 11e and f, at $w = 1.210$ mm where long vertical cracks grew rapidly in other areas,

interfacial cracks were formed and grew along the interface and coalesced with the vertical cracks at the interface. The formation and evolution of interfacial cracks were caused by the large local interfacial stress in the regions surrounding the vertical crack tips [33, 34]. However, no visible interfacial delamination occurred in the coating until the final failure, which indicated the excellent interfacial adhesion of the vacuum-annealed coating.

Figure 12 compares the cross-sectional microstructures of the original and vacuum-annealed coatings after bending. As shown in Fig. 12a, numerous vertical microcracks are formed in the original coating upon bending. These

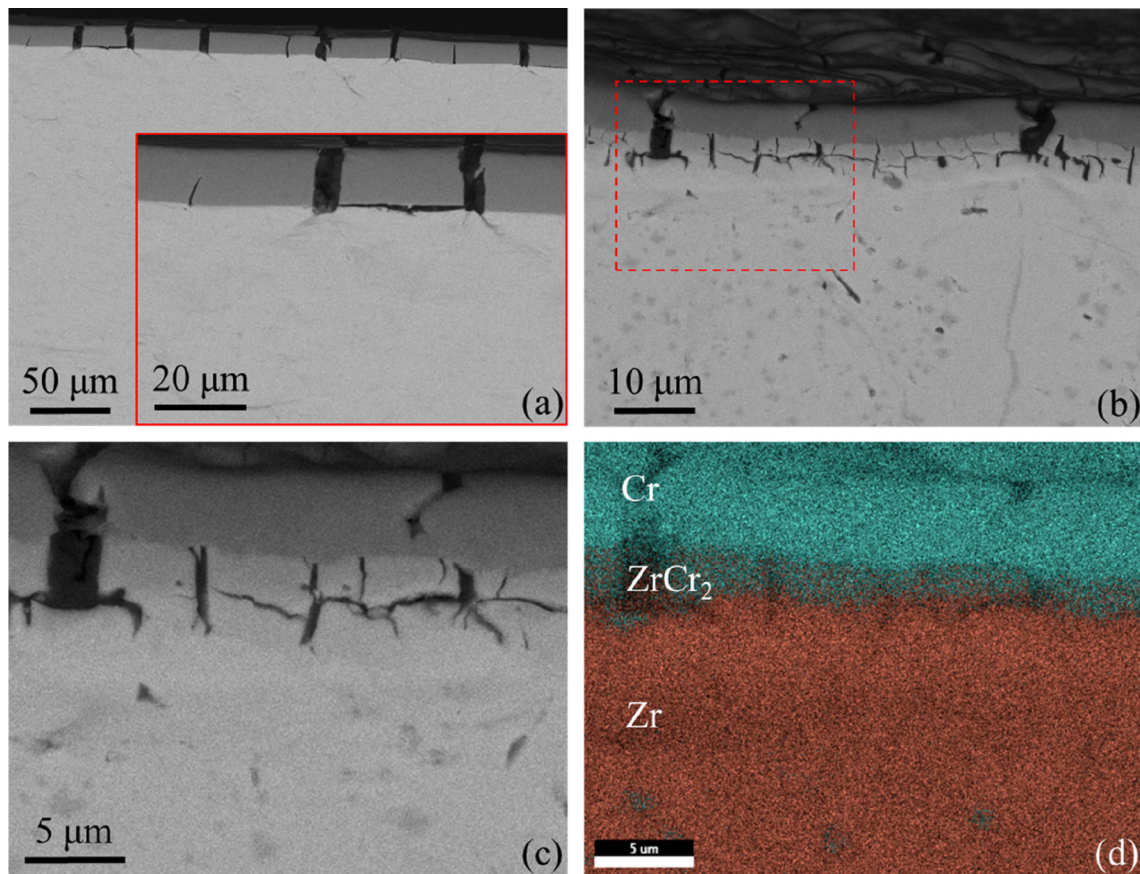


Fig. 12 (Color online) Cross-sectional microstructures of the **a** original and **b** vacuum-annealed coatings after three-point bending tests, **c** the magnified view, and **d** the corresponding EDS map of (c)

cracks primarily formed at the interface, as shown in Fig. 12a. The large number of vertical cracks reflect the high brittleness of the as-deposited coating. In addition, it was found that some interfacial microcracks formed and grew along the interface. As shown in Fig. 12a, some interfacial cracks coalesced with the vertical cracks. The formation and growth of interfacial cracks were due to the large local interfacial stress. As shown in Figs. 12b–d, for the annealed Cr coating, microcracks were mainly formed in the ZrCr_2 layer. In addition, based on the EDS map in Fig. 12d, these cracks also penetrated somewhat into the substrate, which may be because of the thin $\alpha\text{-Zr(O)}$ layer that embrittled the substrate beneath the ZrCr_2 layer. Moreover, several horizontal interfacial cracks lay at the ZrCr_2/Zr interface, illustrating that the ZrCr_2/Zr interfacial adhesion was lower than that for Cr/ZrCr_2 . Furthermore, comparing Figs. 12a and b, despite the numerous cracks at the interface, the annealed coating had fewer vertical cracks than the as-deposited coating, which indicated that high-temperature annealing significantly improved the crack resistance of the Cr coating. Upon annealing, recrystallization in the coating not only released a substantial amount of internal stress, but also altered the grain

morphology of the coating. In Fig. 9, more grain boundaries were found in the equiaxial grains in the direction vertical to the interface, effectively impeding slip deformations in the Cr coating and clogging the propagation of vertical cracks, which could explain why the crack density was substantially reduced in the vacuum-annealed coating.

According to the above results, during high-temperature annealing, the formation of the ZrCr_2 layer caused by interdiffusion embrittled the coating/substrate interface and resulted in numerous microcracks under an external load. Meanwhile, the stress release and grain morphology evolution due to recrystallization significantly enhanced the plasticity of the coating and improved the deformation compatibility, which remarkably improved its crack resistance. For the Cr coating annealed for an extended time, microcracking at the interface could presumably be more remarkable in a thicker diffusion layer, and the vertical crack density in the coating will increase under external loading, despite a decrease in residual stress (see Fig. 6). This is because the crack resistance of the coating decreased with fewer grain boundaries, while the large local interfacial stress increased (see Fig. 6c). Once the Cr coating is consumed after a long period of diffusing into

the substrate, the vertical cracks are mainly located in the brittle $ZrCr_2$ layer under external loading, which could be regarded as numerous micro-notches for the underlying substrate, causing earlier failure than those uncoated.

4 Conclusion

The Cr-Zr interdiffusion behavior of the 1160 °C vacuum-annealed Cr coatings deposited on the Zr-4 substrate was studied. In addition, the interdiffusion effect on the cracking behavior of the Cr coating was studied via three-point bending tests. The results showed that during vacuum annealing, an intermetallic $ZrCr_2$ layer formed because of the Cr-Zr interdiffusion which grew following a nearly parabolic law with annealing time. The Cr coating was consumed because of the presence of the $ZrCr_2$ layer and Cr precipitation in the substrate. Moreover, the coating/substrate interface became rougher with increasing annealing time owing to the uneven diffusion at the interface. The residual stress in the annealed coating decreased with annealing time, resulting from the decrease in the thermal mismatch stress upon cooling. Based on in situ observations, under external loading, microcracks formed in the brittle $ZrCr_2$ layer. Simultaneously, some interfacial cracks formed and grew at the $ZrCr_2$ /Zr-4 interface because of the large local interfacial stress. Despite the remarkable microcracks in the $ZrCr_2$ layer, the vacuum-annealed Cr coating exhibited improved crack resistance compared to the original coating, which mainly benefited from the formation of recrystallized grains and the elimination of residual stress during annealing.

Author contributions All authors contributed to the study conception and design. Material preparation, data collection, and analysis were performed by Ji-Shen Jiang, Dong-Qing Wang, Ming-Yue Du, and Chen-Xue Wang. The first draft of the manuscript was written by Ji-Shen Jiang and all authors commented on previous versions of the manuscript. All authors read and approved the final manuscript.

References

1. K.A. Terrani, Accident tolerant fuel cladding development: promise, status, and challenges. *J. Nucl. Mater.* **501**, 13–30 (2018). <https://doi.org/10.1016/j.jnucmat.2017.12.043>
2. S.J. Zinkle, K.A. Terrani, J.C. Gehin et al., Accident tolerant fuels for LWRs: A perspective. *J. Nucl. Mater.* **448**(1–3), 374–379 (2014). <https://doi.org/10.1016/j.jnucmat.2013.12.005>
3. S. Chen, X. He, C. Yuan, Recent studies on potential accident-tolerant fuel-cladding systems in light water reactors. *Nucl. Sci. Tech.* **31**, 32 (2020). <https://doi.org/10.1007/s41365-020-0741-9>
4. Z. Tan, J. Cai, Neutronic analysis of silicon carbide cladding accident-tolerant fuel assemblies in pressurized water reactors. *Nucl. Sci. Tech.* **30**, 48 (2019). <https://doi.org/10.1007/s41365-019-0575-5>
5. B. Zhu, X. Ge, S. Wang et al., Activation and pumping characteristics of Ti–Zr–V films deposited on narrow tubes. *Nucl. Sci. Tech.* **32**, 50 (2021). <https://doi.org/10.1007/s41365-021-00880-4>
6. C. Tang, M. Stueber, H.J. Seifert et al., Protective coatings on zirconium-based alloys as accident-tolerant fuel (ATF) claddings. *Corros. Rev.* **35**(3), 141–165 (2017). <https://doi.org/10.1515/corrrev-2017-0010>
7. D.C. Roache, A. Jarama, C.H. Bumgardner et al., Unveiling damage mechanisms of chromium-coated zirconium-based fuel claddings by coupling digital image correlation and acoustic emission. *Mater. Sci. Eng. A* **774**, 138850 (2020). <https://doi.org/10.1016/j.msea.2019.138850>
8. H.G. Kim, I.H. Kim, Y.I. Jung et al., Adhesion property and high-temperature oxidation behavior of Cr-coated Zircaloy-4 cladding tube prepared by 3D laser coating. *J. Nucl. Mater.* **465**, 531–539 (2015). <https://doi.org/10.1016/j.jnucmat.2015.06.030>
9. J. Hazan, A. Gauthier, E. Pouillier, Semi-integral LOCA test of cold-spray chromium coated zircaloy-4 accident tolerant fuel cladding. *J. Nucl. Mater.* **550**, 152940 (2021). <https://doi.org/10.1016/j.jnucmat.2021.152940>
10. E.B. Kashkarov, D.V. Sidelev, M.S. Syrtanov et al., Oxidation kinetics of Cr-coated zirconium alloy: effect of coating thickness and microstructure. *Corros. Sci.* **175**, 108883 (2020). <https://doi.org/10.1016/j.corsci.2020.108883>
11. H. Liu, Y. Feng, P. Li et al., Enhanced plasticity of the oxide scales by in-situ formed Cr_2O_3 /Cr heterostructures for Cr-based coatings on Zr alloy in 1200°C steam. *Corros. Sci.* **184**, 109361 (2021). <https://doi.org/10.1016/j.corsci.2021.109361>
12. J.C. Brachet, E. Rouesne, J. Ribis et al., *Corros. Sci.* **167**, 108537 (2020). <https://doi.org/10.1016/j.corsci.2020.108537>
13. J.C. Brachet, I. Idarraga-Trujillo, M. Flem et al., Early studies on Cr-Coated Zircaloy-4 as enhanced accident tolerant nuclear fuel claddings for light water reactors. *J. Nucl. Mater.* **517**, 268–285 (2019). <https://doi.org/10.1016/j.jnucmat.2019.02.018>
14. J.C. Brachet, M.L. Saux, J. Bischoff et al., Evaluation of Equivalent Cladding Reacted parameters of Cr-coated claddings oxidized in steam at 1200 °C in relation with oxygen diffusion/partitioning and post-quench ductility. *J. Nucl. Mater.* **533**, 152106 (2020). <https://doi.org/10.1016/j.jnucmat.2020.152106>
15. H. Yeom, B. Maier, G. Johnson et al., High temperature oxidation and microstructural evolution of cold spray chromium coatings on Zircaloy-4 in steam environments. *J. Nucl. Mater.* **526**, 151737 (2019). <https://doi.org/10.1016/j.jnucmat.2019.151737>
16. J. Yang, U. Stegmaier, C. Tang et al., High temperature Cr-Zr interaction of two types of Cr-coated Zr alloys in inert gas environment. *J. Nucl. Mater.* **547**, 152806 (2021). <https://doi.org/10.1016/j.jnucmat.2021.152806>
17. X. Hu, C. Dong, Q. Wang et al., High-temperature oxidation of thick Cr coating prepared by arc deposition for accident tolerant fuel claddings. *J. Nucl. Mater.* **519**, 145–156 (2019). <https://doi.org/10.1016/j.jnucmat.2019.01.039>
18. T. Wei, R. Zhang, H. Yang et al., Microstructure, corrosion resistance and oxidation behavior of Cr-coatings on Zircaloy-4 prepared by vacuum arc plasma deposition. *Corros. Sci.* **158**, 108077 (2019). <https://doi.org/10.1016/j.corsci.2019.06.029>
19. J.S. Jiang, H.L. Zhai, P.F. Gong et al., In-situ study on the tensile behavior of Cr-coated zircaloy for accident tolerant fuel claddings. *Surf. Coat. Tech.* **394**, 12547 (2020). <https://doi.org/10.1016/j.surfcoat.2020.125747>
20. J. Jiang, D. Zhan, J. Lv et al., Comparative study on the tensile cracking behavior of CrN and Cr coatings for accident-tolerant fuel claddings. *Surf. Coat. Technol.* **409**(1–3), 126812 (2021). <https://doi.org/10.1016/j.surfcoat.2020.126812>
21. J. Jiang, M. Du, Z. Pan et al., Effects of pre-oxidation and interdiffusion on the fracture mechanisms of Cr-coated Zr-4 alloys: an

- in situ three-point bending study. *Mater. Des.* **212**, 110168 (2021). <https://doi.org/10.1016/j.matdes.2021.110168>
22. X. Ma, H. Zhai, F. Meng et al., Benefit or harm of accident tolerant coatings on the low-cycle fatigue properties of Zr-4 cladding alloy: in-situ studies at 400°C. *J. Nucl. Mater.* **545**, 152651 (2021). <https://doi.org/10.1016/j.jnucmat.2020.152651>
 23. L. Nicolai, R. Tendler, Chromium diffusion in zircaloy-4 interface. *J. Nucl. Mater.* **82**, 439–443 (1979). [https://doi.org/10.1016/0022-3115\(79\)90027-8](https://doi.org/10.1016/0022-3115(79)90027-8)
 24. D. Arias, J. Abriata, The Cr-Zr (Chromium-Zirconium) system. *Bullet alloy phase diag* **7**, 237–244 (1986). <https://doi.org/10.1007/BF02868997>
 25. C. Lin, H. Ruan, S. Shi, Mechanical–chemical coupling phase-field modeling for inhomogeneous oxidation of zirconium induced by stress–oxidation interaction. *npj Mater. Degrad.* (2020). <https://doi.org/10.1038/s41529-020-00125-6>
 26. K. Foster, J.E. Hightower, R.G. Leisuret et al., Elastic moduli of the C15 Laves-phase materials TaV₂, TaV₂H(D)_x and ZrCr₂. *Philos. Mag. B* **80**(9), 1667–1679 (2000). <https://doi.org/10.1080/13642810008205755>
 27. J.P. Schillé, Z.L. Guo, N. Saunders, (2001) JMatPro Application Programming Interface Version6.0, Sente Software Ltd <https://www.sentesoftware.co.uk/jmatpro>.
 28. U. Holzwarth, H. Stamm, Mechanical and thermomechanical properties of commercially pure chromium and chromium alloys. *J. Nucl. Mater.* **300**, 161–177 (2002). [https://doi.org/10.1016/S0022-3115\(01\)00745-0](https://doi.org/10.1016/S0022-3115(01)00745-0)
 29. C. Meng, L. Yang, Y. Wu et al., study of the oxidation behavior of CrN coating on Zr alloy in air. *J. Nucl. Mater.* **515**, 354–369 (2019). <https://doi.org/10.1016/j.jnucmat.2019.01.006>
 30. S. Frechin, A.F. Gourgues, T. Forgeron, Transformation-induced plasticity in Zircaloy-4. *Adv. Mech. Behav. Plast. Damag* **3**, 829–834 (2000)
 31. F.D. Fischer, G. Reisner, E. Werner et al., A new view on transformation induced plasticity (TRIP). *Int. J. Plasticity* **16**(7–8), 723–748 (2000). [https://doi.org/10.1016/S0749-6419\(99\)00078-9](https://doi.org/10.1016/S0749-6419(99)00078-9)
 32. J. Huang, S. Zou, W. Xiao et al., Influences of arc current on microstructure of Cr coating for Zr-4 alloy prepared by multi-arc ion plating via EBSD. *Mater. Charact.* **178**, 111211 (2021). <https://doi.org/10.1016/j.matchar.2021.111211>
 33. J. Jiang, X. Ma, B. Wang, Stress analysis of the thermal barrier coating system near a cooling hole considering the free-edge effect. *Ceram. Int.* **46**, 331–342 (2020). <https://doi.org/10.1016/j.ceramint.2019.08.267>
 34. C.H. Hsueh, C.R. Luttrell, S. Lee et al., Interfacial peeling moments and shear forces at free edges of multilayers subjected to thermal stresses. *J. Am. Ceram. Soc.* **89**(5), 1632–1638 (2006). <https://doi.org/10.1111/j.1551-2916.2006.00924.x>